Advances in Water Resources 206 (2025) 105101

Contents lists available at ScienceDirect

Advances in Water Resources

journal homepage: www.elsevier.com/locate/advwatres

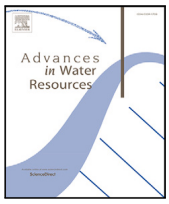

# Gravity currents and wall behavior modeling at high Reynolds numbers

Antonio Ammendola [a,*], Michele Rebesco [b], Federico Falcini [c], Stefano Salon [b], Federico Roman [d]

[a] Department of Mathematics, Computer Science, and Geosciences, University of Trieste, Piazzale Europa 1, 34127, Trieste, Italy
[b] National Institute of Oceanography and Applied Geophysics - OGS, Borgo Grotta Gigante, 42/c, 34010, Sgonico (TS), Italy
[c] Institute of Marine Sciences - National Research Council (ISMAR-CNR), Via del Fosso del Cavaliere, 100, 00133, Roma, Italy
[d] Department of Engineering and Architecture, University of Trieste, Piazzale Europa 1, 34127, Trieste, Italy

ARTICLE INFO

*Keywords:*
Gravity currents
Large Eddy simulations
Wall-functions

ABSTRACT

Gravity currents are buoyancy-driven flows governed by horizontal density gradients, originating from both natural and anthropogenic sources. They play a critical role in a variety of environmental and geophysical processes, and their interaction with human-made structures can be highly significant. These flows are often studied numerically using advanced techniques such as Large Eddy Simulation (LES), which are capable of capturing the complex physics involved. However, the high computational cost associated with LES makes the study of realistic cases prohibitively expensive. To address this challenge, the present study investigates the use of coarse-grid simulations, both with and without wall-model implementations, to evaluate the potential for reducing computational costs while maintaining reasonable accuracy. Gravity currents were analyzed using the lock-exchange configuration at a Reynolds number of 136,000, based on the bulk velocity and the domain height. The analyses indicate that the coarse-grid cases are able to qualitatively reproduce the main characteristics of the current. In one case, based on a wall modification of the eddy viscosity, the front evolution, during the self-similar phase, exhibits an error of 0.25% relative to a wall-resolved reference case. Generally, cases with an eddy viscosity wall models perform better during the self-similar phase and in representing the head of the current, whereas cases without eddy viscosity modification perform better in capturing the integral quantities of a gravity current. Overall, the use of coarser grids reduces computational costs by approximately two order of magnitude while preserving the main characteristics of the gravity current.

## 1. Introduction

Gravity currents are buoyancy-driven flows governed by horizontal density gradients. These gradients could be due to anthropogenic or natural causes. The human activities that can frequently generate gravity currents are for example heavy oil spills (where the change in density is caused by the release of a heavier fluid into a basin of fresh or salty water), increased salinity levels resulting from desalination plants, intrusion of salty water in the coastal water reservoirs, or the filling of hydraulic reservoirs within hydroelectric energy systems (Fannelop and Waldman, 1972; Stancanelli et al., 2017; Chowdhury and Testik, 2014; Hogg et al., 2015). Natural processes that could generate horizontal density gradients include thermohaline and turbidity currents. In thermohaline currents, density differences that drive motion arise from temperature and salinity gradients (Kuhlbrodt et al., 2007), whereas, in turbidity currents, the higher density of the fluid is due to suspended sediments (Meiburg and Kneller, 2010). This phenomenon occurs, for example, when sediments detach from the continental slope in marine environments, leading to underwater sediment movement (Normandeau et al., 2019), or during river flood waves that transport large volumes of sediment into the sea (Sequeiros, 2012; Heerema et al., 2022). The study of gravity currents is fundamental due to their involvement in several critical processes. For instance, in the case of natural processes, thermohaline currents play a significant role in regulating the Earth's global climate by transporting heat from equatorial regions to the poles, thereby influencing both global and local climates. Alterations in these currents can lead to substantial climatic shifts. A deeper understanding of these phenomena is crucial for advancing our knowledge of climate change mechanisms. Moreover, thermohaline currents play a significant role in sediment distribution, contributing to the formation of hydrocarbon reservoirs, similarly to turbidity currents. High-velocity sediment transport processes, such as those driven by turbidity currents, can also lead to substantial seabed morphological changes. These changes pose potential risks to seafloor

* Corresponding author.
*E-mail address:* aammendola@ogs.it (A. Ammendola).

https://doi.org/10.1016/j.advwatres.2025.105101
Received 6 June 2025; Received in revised form 15 August 2025; Accepted 29 August 2025
Available online 4 September 2025

infrastructure, including submarine pipelines, oil and gas platforms, and underwater cables (Rebesco et al., 2014; Gong et al., 2018).

Gravity currents are complex and multifaceted phenomena. Ideally, focusing on certain key aspects, their dynamics are influenced by several factors: the release volume (whether constant or variable), the initial shape of the current, the inertial or viscous nature of the flow, the properties of the ambient fluid (homogeneous or stratified), the density difference between the two fluids, geometric constraints, which in turn affect whether the flow behaves in a two-dimensional or three, dimensional manner, and the characteristics of the bottom boundary (such as slope and roughness). For a comprehensive overview, see for example, Ungarish (2009). Referring to the canonical case of a two-dimensional, inertial gravity current resulting from the release of a finite volume over a horizontal surface, the initial stage is characterized by an acceleration phase, during which potential energy is converted into kinetic energy. Subsequently, the propagation of the gravity current is typically divided into three distinct regimes. In the first regime, known as the slumping phase, the front of the current advances at a constant velocity, and the flow can be considered inviscid. This phase ends when entrainment begins, and the lighter fluid starts mixing with the heavier fluid. Such interaction alters the flow, causing a reduction in the front velocity (self-similar phase). Eventually, the current slows down enough for viscosity to significantly affect the motion (viscous phase), leading to a further decrease in velocity. This overall behavior of the current is consistently treated in Rottman and Simpson (1983), Simpson (1997) and Huppert and Simpson (1980). Usually, the mechanisms involved in the evolution of gravity currents in time are investigated using laboratory (Adduce et al., 2012; Maggi et al., 2022, 2023) and numerical experiments (Georgoulas et al., 2010; Tokyay et al., 2011; Ottolenghi et al., 2016a, 2017; Inghilesi et al., 2018).

The laboratory approach is highly beneficial for directly observing the dynamics of gravity currents. In particular, the lock-exchange experiment offers a controlled setup to simulate natural and anthropogenic density flows, such as turbidity currents, enabling precise observation of mixing and entrainment processes. It consists of a tank filled with two fluids of different densities, separated by a movable barrier. When the barrier is removed, the heavier fluid is released and slides beneath the lighter fluid, generating horizontal pressure gradients that regulate the motion. It is representative of a wide range of phenomena involving the movement of a heavier fluid beneath a lighter one, including the rapid discharge of dense gases into the atmosphere, the interaction between freshwater and saltwater during the opening of a navigation gate, and the sediment mobilization triggered by submarine landslides (Kneller and Buckee, 2000). This facilitates the study of the phenomenon under various conditions, including different density gradients, slopes, domain sizes, and sediment particle dimensions. Such experimental setups enable detailed analysis of entrainment and mixing processes that occur in natural environments. Moreover, laboratory experiments are crucial for accurately calibrating and validating numerical simulations.

Typically, laboratory experiments yield two-dimensional data, along the horizontal and vertical directions, obtained through techniques such as Particle Image Velocimetry (PIV) (Buchhave, 1992). High-precision three-dimensional methods, such as volumetric PIV, are also available. However, as highlighted in the review by Westerweel et al. (2013), their application can be challenging in contexts such as gravity or turbidity currents, due to factors including the possible low transparency of the fluid, the presence of surface undulations, and the occurrence of complex structures such as Kelvin–Helmholtz billows developing at the interface between fluids of different densities.

On the other hand, the numerical approach provides detailed information about the main flow parameters (e.g., velocity, density, salinity) in all directions of motion and at every point in the domain. Moreover, the extensive amount of data collected through numerical simulations enables detailed statistical analysis, facilitating a deeper understanding of the phenomena. Starting from the Navier–Stokes equations, various numerical approaches can be used to tackle the problem. The direct numerical solution of the equations (DNS) is a powerful tool for accurately understanding the physics of a problem, since all scales of motion must be properly resolved in space and time. On the other hand, the computational cost is estimated to scale proportionally with $Re^{3.5}$ (Piomelli, 2001). In environmental contexts, Reynolds numbers are on the order of $10^5$ to $10^6$, for example gravity currents are characterized by Reynolds number of 105 000 (Miramontes et al., 2020), which means that DNS can only be used for academic cases and at low Reynolds numbers (Härtel et al., 2000). To overcome the issue of computational cost and thus be able to simulate cases of practical interest, one can resort to solving the Unsteady Reynolds-Averaged Navier–Stokes (URANS) equations (Georgoulas et al., 2010). In this case, the approach requires the use of a turbulence model to close the system of equations. The model requires significant calibration depending on the type of problem being analyzed, potentially leading to less accurate solutions. A good compromise between the two approaches discussed above is the use of Large Eddy Simulation (LES). In this case, the filtered version of the Navier–Stokes equations is solved. This approach has the advantage of a lower computational cost compared to DNS and provides more accurate insights into the physics of the problem than URANS. Here too, a turbulence model is required to close the system of equations, but it is only used to represent the effects of motion scales smaller than the computational grid size (Sub-Grid Stress, SGS), while the larger scales, responsible for energy transport and mixing, are directly resolved. The advantage of this model lies in its tendency to be universal and independent of the specific problem being analyzed. In fact, the small-scale motions that are not directly resolved tend to exhibit isotropic behavior that is independent of the problem's geometry (Comte and Lesieur, 1996). Nevertheless, applying LES to problems characterized by wall-bounded flow is challenging. Near-wall eddies need to be directly resolved, as they are important for energy transport, and they scale in terms of wall units, i.e., as the Reynolds number increases, the size of the eddies decreases rapidly, leading to a corresponding reduction in the required grid resolution. The proper solution of this layer has a computational cost proportional to $Re^{1.8}$ in space and proportional to $Re^{0.6}$ in time according to Chapman (1979). In practice, LES has a cost similar to that of DNS near a wall. Therefore, even in this case, its application at high Reynolds numbers is not feasible. Some examples of Wall-Resolved Large Eddy Simulations (WR-LES) can be found in Tokyay et al. (2011), Wu and Ouyang (2020), Goodarzi et al. (2020) and Kyrousi et al. (2018).

A strategy to overcome the computational cost associated with resolving the wall layer is to combine LES with Wall Functions (WF-LES). For a review of the method, see Piomelli (2001). In this approach, a coarse grid is used near the wall, which brings obvious computational advantages. The wall structures are not resolved directly, but their effect on the flow is represented, for example, by using approximate boundary conditions or by enhancing the eddy viscosity, relying on the universal law of the wall. The method originated in the context of RANS and was later successfully applied to LES, despite LES being inherently unsteady, whereas wall functions are only valid in a time-averaged sense. Their applicability in the context of LES lies in the fact that, at the first off-wall cell, a wide range of eddies are not resolved, therefore, in this region, LES behaves more like a RANS model (Piomelli, 2008).

As described above, in the initial phase the gravity current behaves as inviscid, and the effect of the wall is not initially significant; later, in addition to an important mixing phase, the development of a bottom boundary layer is expected. This layer evolves in both space and time and requires a high computational cost to be accurately simulated.

The purpose of the present study is to assess whether the use of coarse grids, particularly in the near-wall region, can yield results that are qualitatively comparable to those obtained using a WR-LES. Wall functions will also be employed in this evaluation. To address the problem, the focus is placed on the lock-exchange configuration over a flat bottom. Initially, reference is made to the case analyzed by Ottolenghi

et al. (2016a) in order to validate the numerical tool. The study is then conducted on a case characterized by a high Reynolds number, which is more representative of real phenomena. Several computational grids are employed, including one sufficiently fine to meet the requirements of a WR-LES, whose results serve as a reference. Obtaining qualitatively acceptable results with coarse grids could facilitate the analysis of more complex problems like, for example, geostrophic submarine gravity currents or pyroclastic waves.

The study is organized into four main sections, in addition to the Introduction. First, the numerical model used is explained, including the key characteristics of the Wall Functions. This is followed by a description of the case studies. Next, the results are presented in two parts: the validation of the code, focusing on flow topology, wall shear stresses, and near-wall physics, and an analysis of the High Reynolds cases, comparing WR-LES and WF-LES results. Finally, the study concludes with a summary of the findings.

## 2. Mathematical model

The cases are analyzed numerically, solving the filtered version of the Navier–Stokes equations in the Boussinesq form (continuity and momentum conservation) and a transport equation for a scalar, salinity in this case:

$$\frac{\partial \bar{u}_j}{\partial x_j} = 0 \tag{1}$$

$$\frac{\partial \overline{u_i}}{\partial t} + \frac{\partial \overline{u_j u_i}}{\partial x_j} = -\frac{1}{\rho_0}\frac{\partial \overline{p}}{\partial x_i} + \frac{\partial}{\partial x_j}\left(\nu \frac{\partial \overline{u_i}}{\partial x_j}\right) - \frac{\rho'}{\rho_0} g \delta_{ij} - \frac{\partial \tau_{ij}}{\partial x_j} \tag{2}$$

$$\frac{\partial \bar{s}}{\partial t} + \frac{\partial \bar{u}_j \bar{s}}{\partial x_j} = \frac{\partial}{\partial x_j}\left(k_s \frac{\partial \bar{s}}{\partial x_j}\right) - \frac{\partial \lambda_j}{\partial x_j} \tag{3}$$

the over-bar ($\bar{\square}$) represents filtered values, $u_i$ is the velocity component in the $x_i$ direction, and direction 1, 2 and 3 correspond to $x$, $y$ and $z$ in a cartesian frame of reference. $p$ is the hydrodynamic pressure and $s$ is the salinity concentration, $g$ is gravity, $\delta_{ij}$ is the Kronecker delta, the kinematic viscosity and the molecular diffusivity of the scalar $s$ are $\nu$ and $k_s$, respectively. $\rho'$ is the variation of density with respect to the reference value $\rho_0$, in isothermal conditions, the state equation is:

$$\rho = \rho_0[1 + \beta(s - s_0)] \tag{4}$$

where $\beta$ is the salinity contraction coefficient, $s_0$ is the salinity concentration of the ambient fluid. $\tau_{ij}$ and $\lambda_j$ in Eq. (2) and (3) are the SGS momentum and salinity fluxes, obtained by the following relations:

$$\tau_{ij} = -2\nu_t \bar{S}_{ij} \tag{5}$$

$$\lambda_j = -\kappa_t \frac{\partial \bar{s}}{\partial x_j} \tag{6}$$

where $\bar{S}_{ij}$ is the strain tensor of the solved stresses:

$$\bar{S}_{ij} = \frac{1}{2}\left(\frac{\partial \bar{u}_i}{\partial x_j} + \frac{\partial \bar{u}_j}{\partial x_i}\right) \tag{7}$$

the eddy viscosity, $\nu_t$, and the eddy diffusivity, $\kappa_t$, are defined as:

$$\nu_t = C\Delta^2|\bar{S}| \tag{8}$$

$$\kappa_t = C_s\Delta^2|\bar{S}| \tag{9}$$

where

$$|\bar{S}| = \sqrt{2\bar{S}_{ij}\bar{S}_{ij}} \tag{10}$$

$\Delta$ is the length scale of the LES filter, associated with the grid cell size. The constants $C$ and $C_s$ of Eqs. (8) and (9) are calculated using the WALE (Wall-Adapting Local Eddy-Viscosity) SGS model approach (waleSGS), described in Franck and Ducros (1999). It provides a wall-adaptive representation of the subgrid-scale viscosity, taking into account the specific characteristics of the turbulence near the boundaries. The use of the WALE subgrid-scale model in the context of Wall-Modeled Large Eddy Simulations has been extensively examined in the literature (see, for example, Temmerman et al. (2003) and Mukha et al. (2019)), as well as in more recent applications involving complex flows (De Vanna et al., 2022; Fan et al., 2024).

The model is implemented in the OpenFOAM® environment, starting from the *buoyantBoussinesqPimpleFoam* solver. A finite-volume implementation of the governing equations is carried out implicitly, using the PISO algorithm (Ferziger et al., 2020). The diffusive term is projected using the Euler-Implicit scheme to avoid the diffusive stability limit. The Schmidt number ($Sc = \nu/k_s$) is equal to 600, a reference value for salty water. At $t = 0$, the flow field is at rest in all the domain.

### 2.1. Wall functions

Compared to Direct Numerical Simulation (DNS), the LES approach, which directly solves only the energy-carrying scales, significantly reduces mesh resolution while still delivering appreciable results (Piomelli, 2008). However, in the near-wall region ($y^+ < 11$, with $y^+ = yu_\tau/\nu$, where $u_\tau$ is the friction velocity, and $y$ is the bottom normal coordinate), the flow is characterized by small, energetic structures, that require a high cell density to be appropriately resolved, making LES in this region a $quasi - DNS$. This requirement leads to a prohibitive computational cost at high Reynolds numbers.

The near-wall region's main flow characteristics can be modeled using wall functions to address this issue and reduce computational costs. This methodology originated in the RANS framework and has been successfully extended to LES. For a general review of the method, see Piomelli (2001). There are several methods for the Wall Functions implementation, in the present paper three of it will be taken in consideration: two of them, the Spalding (1961) and the Blended (Spalding, 1961; Menter, 1994) wall function, are based on a constraint of the eddy viscosity ($\nu_t$) at the near wall region, the third (Jayatilleke wall function) is based on the modeling of the eddy diffusivity (Jayatilleke, 1966).

In particular, the Spalding wall function is based on the relation:

$$y^+ = u^+ + \frac{1}{E}[exp(ku^+) - 1 - ku^+ - 0.5(ku^+)^2 - \frac{1}{6}(ku^+)^3] \tag{11}$$

where $u^+ = u/u_\tau$ is the dimensionless velocity near the wall, $k$ is the von Kármán constant, equal to 0.41, and E is the wall roughness parameter, set as 9.8 for smooth walls. Then, the total viscosity, the sum of the molecular and the turbulent components, is calculated as a function of $y^+$ as:

$$\nu_{tot} = \frac{u_\tau y}{\frac{1}{k}\ln Ey^+} = \frac{y^+\nu}{\frac{1}{k}\ln Ey^+} = \nu_t + \nu \tag{12}$$

assuming that the molecular viscosity is proportional to the eddy viscosity:

$$\nu_t = \nu\left(\frac{ky^+}{\ln Ey^+} - 1\right) \tag{13}$$

The Blended wall function uses a different approach for the calculation of $y^+$:

$$y^+ \ln Ey^+ - \frac{kyu_{wall}}{\nu} = 0 \tag{14}$$

where $u_{wall}$ is the velocity in the first off-wall cell. $\nu_t$ is expressed as a function of $u_\tau$ in the following way:

$$\nu_t = max\left(0, \frac{u_\tau^2}{|\nabla u| + \zeta} - \nu\right) \tag{15}$$

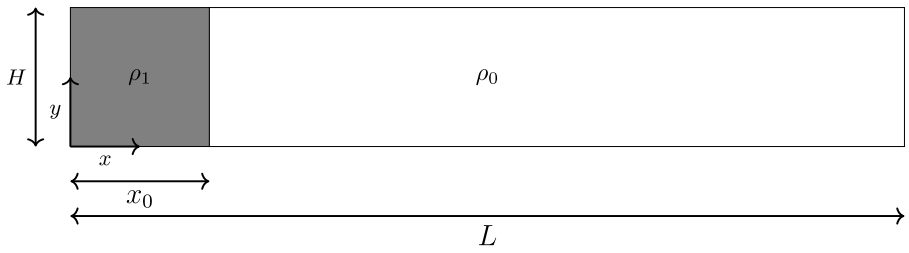


**Fig. 1.** Lock-exchange configuration.

where $\zeta$ is a parameter to avoid the floating number exception during the solver run. $u_\tau$ is dependent on $y^+$, as:

$$\begin{cases} u_\tau = (u^n_{\tau_{vis}} + u^n_{\tau_{log}})^{\frac{1}{n}} \\ u_{\tau_{vis}} = \dfrac{u_{wall}}{y^+} \quad y^+ < 30 \\ u_{\tau_{log}} = k\dfrac{u_{wall}}{\ln E y^+} \quad y^+ > 30 \end{cases} \tag{16}$$

where $u_{\tau_{vis}}$ is the friction velocity computed by the viscous sublayer assumptions, $u_{\tau_{log}}$ is the friction velocity computed by the inertial sublayer assumptions, and $n$ is a blending exponent.

Finally, the Jayatilleke wall function models the eddy diffusivity. It is based on the calculation of the scalar flux near the wall:

$$\begin{cases} s_{flux} = \rho k_t(\frac{s_{wall}-s_p}{y}) \quad y^+ > y^+_L \\ s_{flux} = \frac{(s_{wall}-s_p)(\rho u_\tau)}{Sc_t(\ln E y^+ + P_j)} \quad y^+ < y^+_L \end{cases} \tag{17}$$

where $y^+_L$ is a threshold value, denoting the intercept between the linear part of the scalar profile and the logarithmic part, dependent on the turbulent Schmidt number($Sc_t = \nu_t/k_t$). $s_{wall}$ and $s_p$ are the salinity concentrations respectively at the wall and out of it. $P_j$ is a parameter of the Jayatilleke model, calculated using the following relation:

$$P_j = 9.24\left[\left(\frac{Sc}{Sc_t}\right)^{\frac{3}{4}} - 1\right]\left[1 + 0.28e^{-0.007(Sc/Sc_t)}\right] \tag{18}$$

By comparing the two $s_{flux}$ equations, it is possible to estimate the eddy diffusivity coefficient $k_t$.

The three models exposed in this chapter will be implemented in the study cases later exposed, to decrease the computational costs for high Re simulations.

## 3. Study cases

The analysis to verify the potential advantage of using coarse grids was conducted on the lock-exchange configuration, see Fig. 1. The domain is a box of height $H$ and length $L$, with a partition wall at a distance $x_0$ from the left wall, which separates two fluids of different densities.

When the partition is removed, due to the horizontal pressure gradient, a flow is triggered, causing the denser fluid $\rho_1$ on the left side of the wall to move along the bottom relative to the surrounding fluid with ambient density $\rho_0$. The possible configurations are characterized in terms of aspect ratio $R$, reduced gravity $g'$ and the Reynolds number $Re$, defined as follows:

$$R = H/x_0 \tag{19}$$

$$g' = g \cdot \frac{\rho_1 - \rho_0}{\rho_0} \tag{20}$$

**Table 1**
Cases with relatives dimensions, mesh resolutions, and Re number.

| Case | L × H × d [m] | *Mesh resolution* | *LES Model* |
|---|---|---|---|
| Ottolenghi et al. 2016 | 4.096 × 0.2 × 0.2 | 2048 × 128 × 64 | *dynamicSGS* |
| Ottolenghi-FR | 4.096 × 0.2 × 0.2 | 2048 × 140 × 64 | *waleSGS* |

$$Re = \frac{u_b H}{\nu} \tag{21}$$

where $u_b$ is the buoyant velocity and is defined as:

$$u_b = \sqrt{g' H} \tag{22}$$

This type of case study is commonly used to analyze the physics of gravity currents through numerical simulations and experiments (see, among others, Tokyay et al., 2011; Ottolenghi et al., 2016a, 2017; Inghilesi et al., 2018). Therefore, it is a valuable tool for assessing the performance of coarse grids with and without wall models in reproducing the main physics of the problem.

First, a validation of the mathematical model was carried out without wall models, i.e., by properly resolving the viscous sub-layer. The comparison is performed against the results of Ottolenghi et al. (2016a), where a Large Eddy Simulation methodology is employed to carry out a series of numerical experiments, designed to replicate and extend physical laboratory observations. This case, identified by Ottolenghi-FR (with FR standing for 'Fully Resolved' case) label, uses the same characteristics as RUN2 and EXP2 of the reference paper: $R = 2$, $g' = 0.29\ \mathrm{m/s^2}$ (calculated in the present cases considering a $\rho_1 = 1030\ \mathrm{kg/m^3}$ and $\rho_0 = 1000\ \mathrm{kg/m^3}$), and $u_b = 0.24$ m/s, resulting in $Re = 48\,522$. Further details are provided in Table 1. The grid spacing is $\Delta x = 0.01H$, $\Delta z = 0.016H$, while $\Delta y$ ranges from $0.01H$ at the center of the domain to $0.002H$ at the boundaries. From a posteriori analysis, using the time dependent maximum wall shear stress during the evolution of the gravity current, we obtain $\Delta x^+ = 50$, $\Delta z^+ = 20$, while $\Delta y^+ = 1$ at the bottom, ensuring a correct solution of the viscous layer.

The application of wall functions requires a particularly coarse grid in all directions in terms of wall units, as discussed in Piomelli (2001). At the same time, an adequate number of points along the wall-normal direction is necessary to properly resolve the boundary layer and the mixing (Cabot and Moin, 2000).

Therefore, the case used for validation, characterized by a low Reynolds number, does not allow the assessment of wall models. To overcome these issues, a configuration with a domain height twice that of the Ottolenghi et al. (2016a) case was considered. In this setup (HR label), the higher Reynolds number results from the elevated potential energy, which is later converted into kinetic energy after the lock release. This adjustment brings the test case closer to the real scale of the phenomenon (with Re on the order of $10^5$, Miramontes et al. (2020)) and is more suitable for wall modeling. The decision to modify the domain characteristics rather than the viscosity was made to allow potential future comparisons with experimental setups.

To provide a reference case, a Fully Resolved simulation, HR-FR, was performed at $Re_b = 136000$. The study by Pelmard et al. (2018) presents, in the context of large-eddy simulation, an analysis

**Table 2**
Cases with relatives dimensions, mesh resolutions, and Re number.

| Case | L × H × d (m) | *Mesh resolution* | $u_b$ (m/s) | $Re_b$ | *Wall approach* |
|---|---|---|---|---|---|
| HR-FR | 4.096 × 0.4 × 0.2 | 2560 × 200 × 92 | 0.34 | 136 000 | *Fully resolved* |
| HR-NR | 4.096 × 0.4 × 0.2 | 1024 × 100 × 48 | 0.34 | 136 000 | *Not resolved* |
| HR-WM-J | 4.096 × 0.4 × 0.2 | 1024 × 100 × 48 | 0.34 | 136 000 | *Jayatilleke Wall Model* |
| HR-WM-S | 4.096 × 0.4 × 0.2 | 1024 × 100 × 48 | 0.34 | 136 000 | *Spalding Wall Model* |
| HR-WM-B | 4.096 × 0.4 × 0.2 | 1024 × 100 × 48 | 0.34 | 136 000 | *Blended Wall Model* |

of grid requirements for gravity currents generated by a lock-exchange configuration over a flat bottom. In particular, the authors simulate a case characterized by $Re_{b,H/2} = 60000$, where in the definition of both the Reynolds number and the bulk velocity, the characteristic length scale is taken as $H/2$. The finest grid employed in the study consists of 3150, 185, and 200 cells in the $x$, $y$, and $z$ directions, respectively. The case analyzed herein, rescaled using $H/2$, yields $Re_{b,H/2} = 48166$, which is of the same order of magnitude as the previously cited case. A computational grid with a resolution of 2560, 200, and 96 cells in the $x$, $y$, and $z$ directions, respectively, is employed. Considering the computational domain adopted, this resolution is greater than, or at least comparable to, that used in Pelmard et al. (2018).

Accordingly, wall-modeled cases (denoted as WM) were simulated on a coarser grid, using the same configuration, as detailed in Section 2.1. The details of the simulations are provided in Table 2. The HR-NR case refers to a simulation performed without wall resolution or wall functions, to highlight the role of the adopted models.

As shown in Table 2, the number of cells in the coarse grids cases is reduced by approximately 90% compared to the fully resolved simulations, with a significant reduction of the computational time (from about $10^2$ h (h) of the HR-FR case to $10^0$ h of the HR-WM-S case, with 320 processors implied for both cases).

To complete the study, additional cases, not reported in Table 2, have been analyzed, varying the grid resolutions in the x, $y$ and z directions. Some findings are referenced only in Sections 4.2.2 and 4.2.4.

## 4. Results

### 4.1. Validation

This section addresses the validation phase, comparing the results obtained from the model presented in Section 2 (Ottolenghi-FR) with the reference results reported by Ottolenghi et al. (2016a) and Ottolenghi et al. (2017).

#### 4.1.1. Flow topology

The evolution of the front position over time allows for the analysis of the gravity current across different regimes. The front, denoted as $x_f$, is defined as the frontmost position of the current nose located 0.02H above the bottom surface, as in Nogueira et al. (2013) and Ottolenghi et al. (2016a). To define the interface between the current and the ambient fluid, a characteristic isopycnal is defined by a threshold value of $\langle \rho^* \rangle = 0.02$, as in Ottolenghi et al. (2016a), where $(\langle\rangle)$ represents the averaging operator in the spanwise direction, while $\rho^*$ is the dimensionless density field calculated as:

$$\rho^* = \frac{\rho(x, y, z, t) - \rho_0}{\rho_1 - \rho_0} \tag{23}$$

Fig. 2 shows a comparison between the results of the Ottolenghi-FR simulation and those of Ottolenghi et al. (2016a,b), both numerical (RUN2) and experimental (EXP2), for the dimensionless front position ($x_f^* = (x_f - x_0)/x_0$) over dimensionless time ($T^* = t \cdot u_b/x_0$), in logarithmic scale. It can be seen that the results obtained with the model presented in Section 2 agree with the reference numerical results and are very similar to the experimental ones. Using the logarithmic scale, the different phases of the gravity current can be easily observed, as described in the introduction. During the slumping phase, the current front velocity remains approximately constant. The curve in this phase displays a linear trend with a unitary slope (dashed dot line with slope = 1 in Fig. 2). This phase also marks the onset of Kelvin–Helmholtz instabilities, as described by Boegman (2009), which are evident in Fig. 3a, where the dimensionless density contour is shown during the initial stage of the current, $T^* = 7.7$. As the current advances, it enters into the so-called self-similar phase; the front begins to decelerate because of the entrainment of ambient fluid into its head (see also Fig. 3c at $T^* = 31.3$). This entrainment alters the slope of the curve, with a progressive transition from $T^*$ to $T^{*2/3}$ (light gray dashed dot line slope = 2/3 in Fig. 2). As the current advances, the front position curve stabilizes with a slope of 2/3. The density field (see Fig. 3c) reveals a thinning of the current, resulting from the continued decline in density concentration. For the analyzed case, due to the adopted aspect ratio and reduced gravity, the domain is too short to observe the viscous phase; in this phase, the front velocity slows down further and the curve slope tends to 1/5 (Rottman and Simpson, 1983).

#### 4.1.2. Wall-shear stresses

Wall stress is an important parameter in evaluating gravity currents, as it provides an indication of the flow's ability to erode the bottom and potentially sustain the gravity current itself. It is defined as:

$$\tau_w = \mu \frac{d\langle u \rangle}{dy}|_{y=0} \tag{24}$$

where $\mu$ is the dynamic viscosity. The friction velocity is related to the wall stress through the following equation:

$$u_\tau = \sqrt{\frac{|\tau_w|}{\rho}} \tag{25}$$

Fig. 4 shows a comparison with the reference data for the friction velocity along the streamwise direction, averaged along the spanwise direction, and non-dimensionalized using the buoyancy velocity $u_b$. The plots refer to two time instants, representative of the self-similar phase described above. Fig. 4a corresponds to $T^* = 31.3$, while Fig. 4b corresponds to $T^* = 65.4$.

The results agree well with the reference data. In both plots, higher values are observed at the head of the gravity current, with peaks near the front, followed by a decrease towards the tail of the current. The higher values at the head are attributed to the structures forming in the mixing layer at the interface between the denser fluid and the ambient fluid, specifically the Kelvin–Helmholtz billows.

It can also be observed that during the transition from the slumping phase to the self-similar phase, the wall stress decreases, leading to a corresponding reduction in the current sediment transport capability.

Additionally, in Fig. 5, the Hövmoller diagrams (which represent the evolution in time of the dimensionless friction velocity trend along the streamwise direction) of Ottolenghi-FR case confirms that in any instance of time, the highest values of friction velocity are observed at the head of the current.

### 4.2. High Reynolds cases and wall models

This section presents the results obtained using coarse grids for the case at $Re = 136,000$ and compares them with a fully resolved simulation.

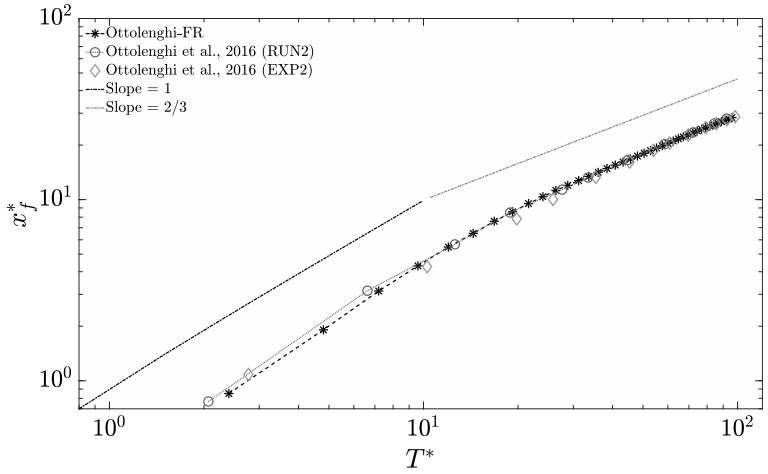


**Fig. 2.** Dimensionless front position evolution in time, in logarithmic scale, comparison between the Ottolenghi-FR case and the Ottolenghi et al. (2016a) results.

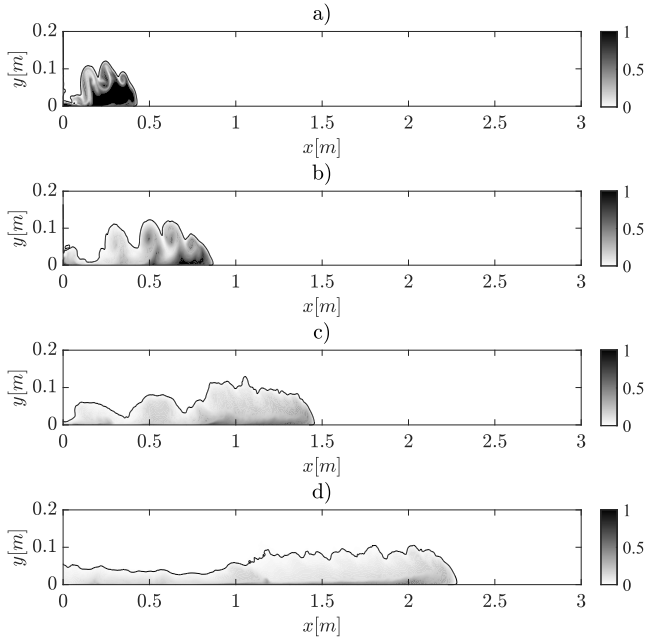


**Fig. 3.** Contour of $\langle \rho^* \rangle$ at different runs for the Ottolenghi-FR case: (a) time $T^* = 7.7$, (b) time $T^* = 18.6$, (c) time $T^* = 31.3$, (d) time $T^* = 65.4$.

#### 4.2.1. Boundary layer

The application of wall models relies on the assumption that a well-defined boundary layer exists and that, in the near-wall region, the flow exhibits a linear profile within the viscous sublayer, followed by a logarithmic profile. In this section, the characteristics of the boundary layer are assessed for the fully resolved case; the analysis was conducted at the head of the current. Various approaches can be employed to define its spatial extent (see, for example, Nogueira et al. (2014)). In the present study, we adopted a definition based on density. For each position i along the $x$-direction, the following quantity was computed:

$$\langle \rho^*_j(i) \rangle = \frac{\sum_{j=1}^{nh} \langle \rho^*(i,j) \rangle \Delta y(j)}{\sum_{j=1}^{nh} \Delta y(j)} \tag{26}$$

where j denotes the wall-normal direction, and $j = nh$ corresponds to the height of the gravity current, evaluated with respect to the reference value $\langle \rho^* \rangle = 0.02$. A mean value was then computed along the $x$-direction over the entire gravity current:

$$\langle \rho^*_{ij} \rangle = \frac{1}{nl} \sum_{i=1}^{nl} \langle \rho^*_j(i) \rangle \tag{27}$$

where $i = nl$ represents the position of the front. The head is a region characterized by high density values; the criterion adopted for its definition was therefore to identify the first occurrence for which $\langle \rho^*_j(i) \rangle < \langle \rho^*_{ij} \rangle$ holds. This criterion was applied starting from the head and moving in the direction opposite to the current. Fig. 6 illustrates, at t = 13 s, the height of the current, the variables described above, and the start and end points of the head as identified by this method.

Within the head region, the velocity profile along the wall-normal direction was computed by first averaging the data in the spanwise direction and subsequently performing an ensemble average over the profiles obtained along $i - direction$. Fig. 7 shows an example of the resulting non-dimensional velocity profile. In addition, the corresponding velocity gradient profile du/dy is presented, together with a representative near-wall behavior consisting of a linear profile, valid in the viscous sublayer ($u^+ = y^+$), and a logarithmic profile of the form $y^+ = A \ln(y^+) + B$ where $A = 1/\kappa = 1/0.41 = 2.439$ and $B = 5.5$. In a $u^+ - \log(y^+)$ plane, these two coefficients correspond, respectively, to the slope and the intercept. From the figure, it can be observed that the first computational point is located at $y^+_1 = 1$, and the first three points lie approximately within the viscous sublayer ($y^+ < 5$); the inner layer then extends to about 20 wall units. This is followed by a logarithmic trend up to approximately 70 wall units. Compared to the canonical logarithmic profile shown, the present case exhibits a steeper slope and a lower intercept. Such behavior is consistent with wall-bounded flows under stratification, as reported, for example, by Armenio and Sarkar (2002), where, in the case of channel flow, increasing stable stratification results in a corresponding increase in the slope A and a reduction in the intercept B, although in their study the deviation occurs downstream of the inner layer.

The regions described above can be analyzed in terms of the velocity gradient $dU/dy$. In a canonical wall-bounded flow under neutrally stratified conditions, the inner layer is characterized by strong vertical velocity gradients, which then tend to attain a nearly constant value within the logarithmic region. At the outer edge of the boundary layer, the velocity gradients approach zero, indicating that the velocity approaches the undisturbed free-stream value. A similar behavior is observed in the present case, see Fig. 7 for the profile of $du/dy$, although the profile is subsequently influenced by the mixing region and the counterflow velocity of the ambient fluid. The criterion adopted to define the thickness of the boundary layer was du/dy = 0.

In addition, the possible extent of the logarithmic profile was also estimated through the quantity $du/d(logy+)$.

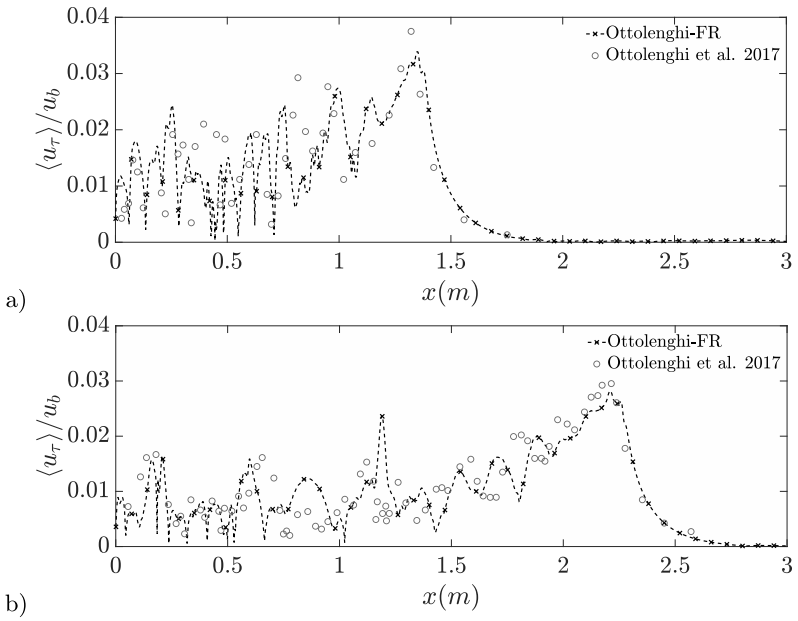


**Fig. 4.** Streamwise evolution of dimensionless friction velocity at different times, a confrontation between Ottolenghi-FR (dashed lines and crosses) and the Ottolenghi et al. (2017) case (dashed lines and circles): (a) time $T^* = 31.3$, (b) time $T^* = 65.4$.

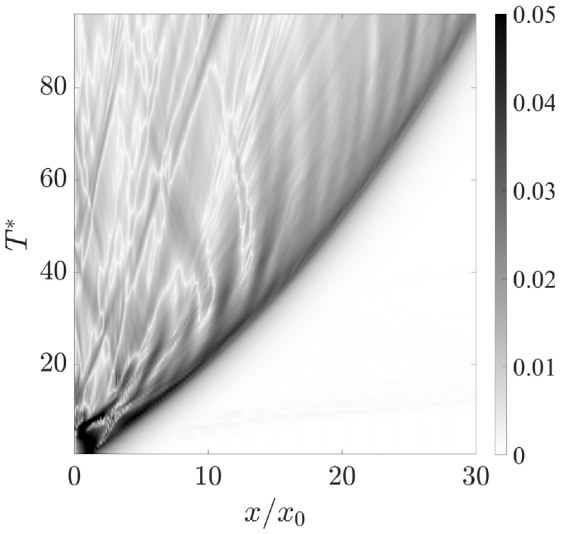


**Fig. 5.** Hövmoller diagrams of the dimensionless friction velocity field for the Ottolenghi-FR case.

Fig. 8 presents the boundary layer height determined and the logarithmic extent at one-second intervals, expressed in non-dimensional terms. The initial instants are not reported, as a strong variability of the profiles is observed along the $x$-direction and the head is not yet well defined. It is observed that during the initial slumping phase, a boundary layer develops and progressively increases in vertical extent, reaching a maximum at approximately six seconds. Subsequently, as mixing processes with the ambient fluid are initiated, the boundary layer thickness decreases towards an asymptotic value.

The logarithmic region initially occupies a limited fraction of the boundary layer; during the self-similar phase, it progressively extends over a larger portion, and in the final phase, it seems to stabilize at a constant value.

#### 4.2.2. Flow topology

The increase in available potential energy, from that corresponding to $H = 0.2$ m to that corresponding to $H = 0.4$ m, results in an acceleration of the flow, as it is possible to observe in Fig. 9. In the validation case, the front position was determined based on a prescribed height, for consistency with the reference study. In the present case, in order to avoid potential ambiguities associated with the choice of a prescribed height, the position of the nose was computed by averaging, along the wall-normal direction, the values of $\langle \rho^* \rangle$.

Fig. 10 compares the front position evolution over time between the Wall-Resolved LES case (HR-FR) and the cases run on a coarser grid. Overall, in the initial stage, the simulations provide similar results. Subsequently, in comparison with the resolved case, it is observed that the HR-WM-B case tends to exhibit a slower evolution of the front. For the other cases, a similar behavior is observed: a slight deceleration in the central phase, followed, in the HR-NR and HR-WM-J cases, by a slight acceleration towards the end of the simulation. The different phases of the motion are described in detail below.

During the slumping phase, both the Wall Function and not resolved cases exhibit behavior comparable to the fully resolved case (HR-FR), characterized initially by a nearly constant front velocity, followed by a gradual decrease between 7 and 10 s. In the self-similar phase, the HR-FR case continues to decelerate, primarily due to the dilution of the saline water into the surrounding freshwater. This deceleration is also observed in all the other cases, although in the HR-WM-B case it is excessively pronounced.

In the final portion of the self-similar phase, the deceleration observed in the resolved case persists and is accurately captured by the HR-WM-S case. Conversely, the other case based on increased eddy viscosity, HR-WM-B, maintains the excessive slowing previously noted. The unresolved case and the one based on the modification of eddy diffusivity, on the other hand, exhibit a slight acceleration of the front compared to the resolved case. In these two cases, the use of a coarse grid leads to an increase in velocity gradients near the wal, compensating for the lower eddy viscosity values in the wall-stress computation.

in Table 3, a quantitative analysis of the coarse grid cases performance relative to the fully resolved case (HR-FR) is presented through the computation of percentage errors. These errors were first evaluated over the entire simulation time and then subdivided into three distinct

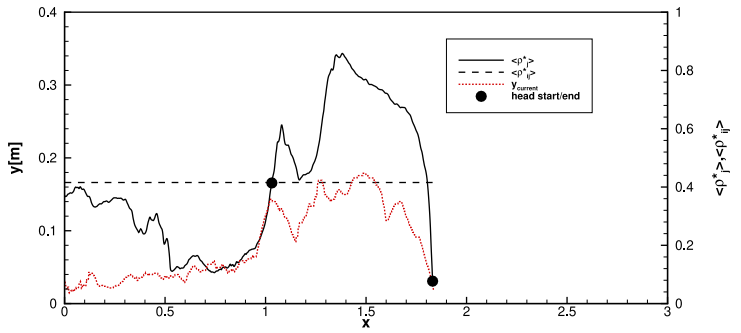


**Fig. 6.** Example of gravity current head identification based on density.

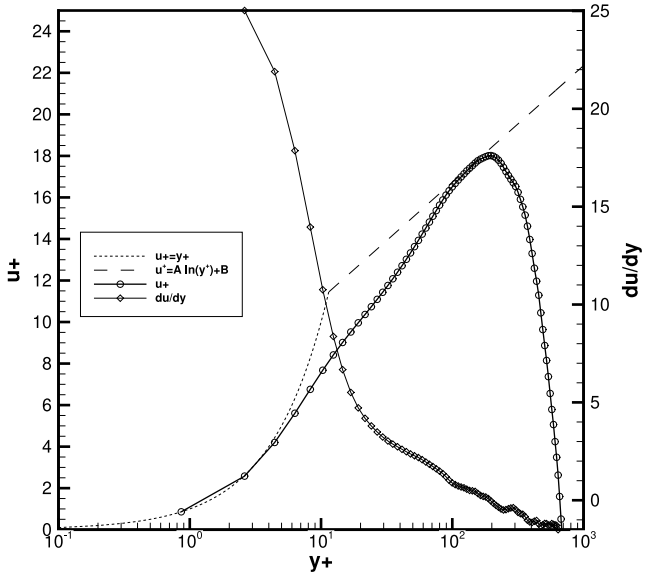


**Fig. 7.** Mean streamwise velocity profile along wall normal direction in non-dimensional form and velocity gradient along wall normal direction.

temporal intervals to assess the model behavior across different flow regimes. This error was computed as follow (Ottolenghi et al., 2016a):

$$Err = mean\left(\left|\frac{x_{f(HR-FR)} - x_{f(WM)}}{x_{f(HR-FR)}}\right|\right) \tag{28}$$

From Table 3, It can be observed that, among the various cases, although the difference with respect to HR-FR is minor (never exceeding 2.70%), all cases perform similarly during the slumping phase ($T^* = 3.4$–$34$). In contrast, in the self-similar phase, the HR-WM-B configuration begins to deviate from the reference case and achieves its peak error between $T^* = 34$ and 102, subsequently decreasing in the final 10 s. The HR-NR configuration, after the initial seconds, maintains an almost constant error trend, oscillating between 0.67% and 0.52% over the last 30 s of the simulation. The HR-WM-J case, namely, the other case without eddy viscosity intensification, exhibits behavior similar to that of HR-NR, except in the final phase, where the error tends to increase slightly. The HR-WM-S case, after a divergence peak from HR-FR between $T^* = 34$ and 102, exhibits only a minimal deviation in the closing seconds (approximately 0.25%). Overall, albeit by a narrow margin, the HR-WM-S configuration achieves the lowest total error among all the cases considered. Moreover, as time progresses, the error exhibits a decreasing trend.

The observed behavior can be interpreted in light of the underlying dynamics of gravity currents. The phenomenon exhibits intrinsic temporal and spatial unsteadiness, which is likewise reflected in the evolution of the wall-bounded flow.

In the initial instants, the flow can be qualitatively approximated as inviscid. A viscous layer develops at the wall; however, the influence of friction has not yet propagated in the wall-normal direction, and the velocity gradients along the vertical are negligible. In this situation, it is to be expected that the use of coarse grids, both with and without wall models, can accurately reproduce the behavior of the flow.

As the current evolves, the viscous effects in the vicinity of the wall become increasingly pronounced, leading to the formation of a boundary layer.

In this case, an accurate representation of the near-wall flow dynamics becomes crucial. In the HR-WM-B case, for example, the excessive wall eddy viscosity results in a deviation from the resolved case. For the other cases, only in the final phase, regarding the evolution of the front, there is a slight improvement observed when employing a wall model.

The analysis also considered other coarse grid configurations (here not shown). It was observed that a reduction in the number of cells along the $x$-direction (from 1024 to 832) leads, for the various cases analyzed, to an overall slowing of the front compared to the resolved case. A reduction in resolution along the $y$-direction (to 60 and 80 cells) determines a different trend between the cases without eddy viscosity intensification, HR-NR and HR-WM-J, and the cases HR-WM-S and HR-WM-B. The former tend to accelerate with respect to the resolved case, whereas the latter tend to decelerate. For the latter cases, the model evidently yields an excessive eddy viscosity at the first off-wall cell. In contrast, for the HR-NR and HR-WM-J cases, the absence of eddy viscosity intensification results in an increased velocity gradient in order to maintain force balance. Finally, an opposite trend is also observed when modifying the resolution in the $z$-direction (32 and 64 cells), albeit to a lesser extent.

Fig. 11 shows, on an xy plane and at four time instants, a contour of the dimensionless density averaged in the spanwise direction for cases HR-FR, HR-NR and HR-WM-S.

As noted in the front-position analysis, the HR-WM-S and HR-WM-NR configurations show slightly better performance than the other cases in terms of front evolution.

Analyzing the shape of the current, it is observed that, in general, the head size is qualitatively captured reasonably well, while the tail appears thicker in the coarse grid cases compared to the reference case. At time $T^* = 23.8$, as shown in Fig. 11a, during the slumping phase, Kelvin–Helmholtz instabilities are visible. Despite the reduced grid resolution, the HR-NR seems to preserve the head shape of the reference case better than HR-WM-S, maintaining it more compact and dense.

At $T^* = 47.6$, as the current progresses, the tail becomes more extended. Here, the HR-WM-S case shows slightly better results compared with the reference case than HR-NR. Indeed, in the HR-NR case, the structures appear sharper and exhibit reduced mixing, particularly near the bottom and close to the front of the current, where the salinity concentration remains higher compared to HR-FR.

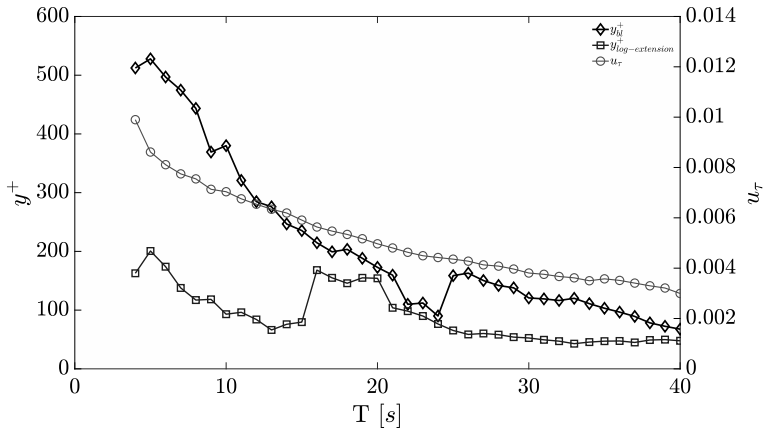


**Fig. 8.** Evolution of the boundary layer and of the friction velocity over time at the head of the gravity current.

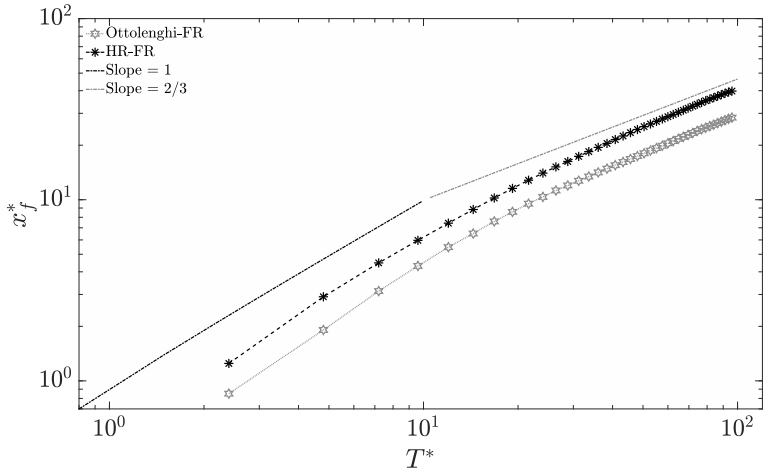


**Fig. 9.** Dimensionless front position evolution in time, comparison between HR-FR(asterisk markers) and Ottolenghi-FR (hexagram markers) cases.

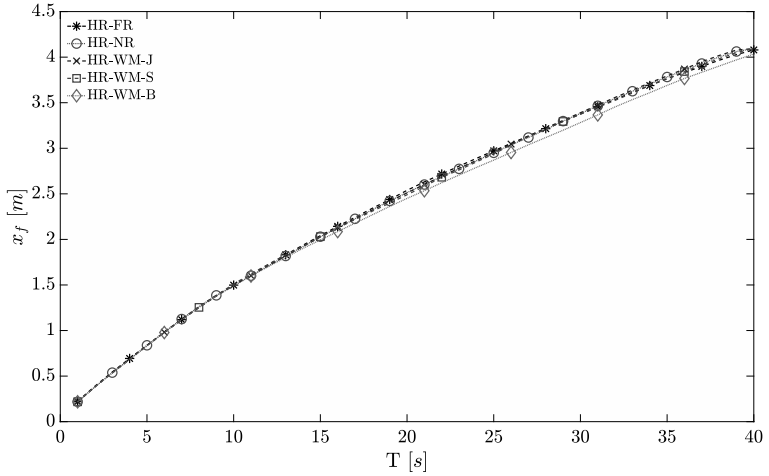


**Fig. 10.** Front position evolution in time, comparison between HR-FR case and the HR case with a coarser mesh.

**Table 3**
Cases with percentage error, in comparison with HR-FR.

| Case | $Err_{tot}\%$ | $Err\%$ ($T^* = 3.4 - 34$) | $Err\%$ ($T^* = 34 - 102$) | $Err\%$ ($T^* = 102 - 136$) |
|---|---|---|---|---|
| HR-NR | 0.71 | 0.95 | 0.67 | 0.52 |
| HR-WM-J | 1.83 | 0.91 | 0.64 | 0.84 |
| HR-WM-S | 0.68 | 1.00 | 0.80 | 0.25 |
| HR-WM-B | 1.88 | 1.00 | 2.70 | 1.94 |

At $T^* = 91.8$, The HR-WM-S case exhibits improved performance in terms of current-head extension and mixing. Unlike HR-NR, it maintains the elongated head shape characteristic of the reference case. This behavior is likely due to the increased viscous contribution to the flow during this simulation phase, which is effectively represented by the Spalding model.

At $T^* = 119$, as viscous effects become more relevant, the current shape in the HR-WM-S case closely matches that of the HR-FR case, whereas HR-NR continues to exhibit a more compact head with reduced mixing with the ambient fluid.

In general, as the current evolves into the self-similar phase ($T^* = 47.6, 91.8, 119$), the differences between the resolved case and the HR-WM-S cases diminish, while the HR-NR case appears to maintain the behavior observed in the slumping phase over time.

#### 4.2.3. Wall-shear stresses

Similarly to what was analyzed during the validation phase, the evolution of wall stress in space and time is evaluated, through the friction velocity, see Eq. (25). This parameter is important because it defines the model's ability to accurately represent potential bed erosion.

Fig. 12a, b, c and d show the trend of the mean friction velocity made non-dimensional with $u_b$, along the streamwise direction at the dimensionless time instants $T^*$ of 23.8, 47.6, 91.8 and 119 respectively, corresponding to the slumping and the self-similar phase.

Unlike Fig. 4, a higher deviation is observed between the coarse grid cases compared to the reference case. On the other hand, this behavior is expected, considering the different numerical schemes adopted near the wall and the grid resolution. Qualitatively, it can be observed that the cases exhibit similar average values, in terms of magnitude, at the head and tail of the gravity current.

During the slumping phase, the coarse-grid cases exhibit peaks that are in phase with the wall resolved case, although lower peak values are observed, particularly for the cases involving eddy viscosity intensification (HR-WM-S and HR-WM-B).

This behavior can be explained by what was previously observed. The slumping phase is strongly characterized by the formation of Kelvin–Helmholtz structures, which are then reflected in the wall stress. In the coarse grid case, these structures are not properly modeled (see Fig. 11a with the density contour and the section on entrainment), and this is reflected in the peaks observed in Fig. 12a. This is particularly true for the HR-WM-S and HR-WM-B cases, where the assumption of a wall-law (valid under steady conditions) also plays a role, whereas the slumping phase is strongly unsteady.

As time progresses and the flow enters the self-similar phase, the friction velocity values decrease. The values obtained with coarse grids are more consistent with the resolved case, at least in the head region of the gravity current, while they tend to deviate with higher values in the tail, as shown in Fig. 12b, and c. This is consistent with the thicker tail observed in the contours of Fig. 11b,c, and d. In particular, a larger deviation is observed for the cases without eddy viscosity intensification (HR-NR and HR-WM-J), whereas a clear slowing of the current is evident in the HR-WM-B case. The observations are confirmed in the final phase (12d); in particular, it is noted that the HR-WM-S case, excluding the tail, tends to be more consistent with the resolved case. It should be recalled that in this phase, this case exhibits the smallest error compared to HR-FR with regard to the evolution of the front.

The general trend of friction velocity over time and space can also be observed in Fig. 13, which presents the Hövmoller diagram for the HR-FR and HR-WM-S cases. The behavior is similar, with the highest values consistently appearing at the head or, during the slumping phase, in correspondence with the Kelvin–Helmholtz structures.

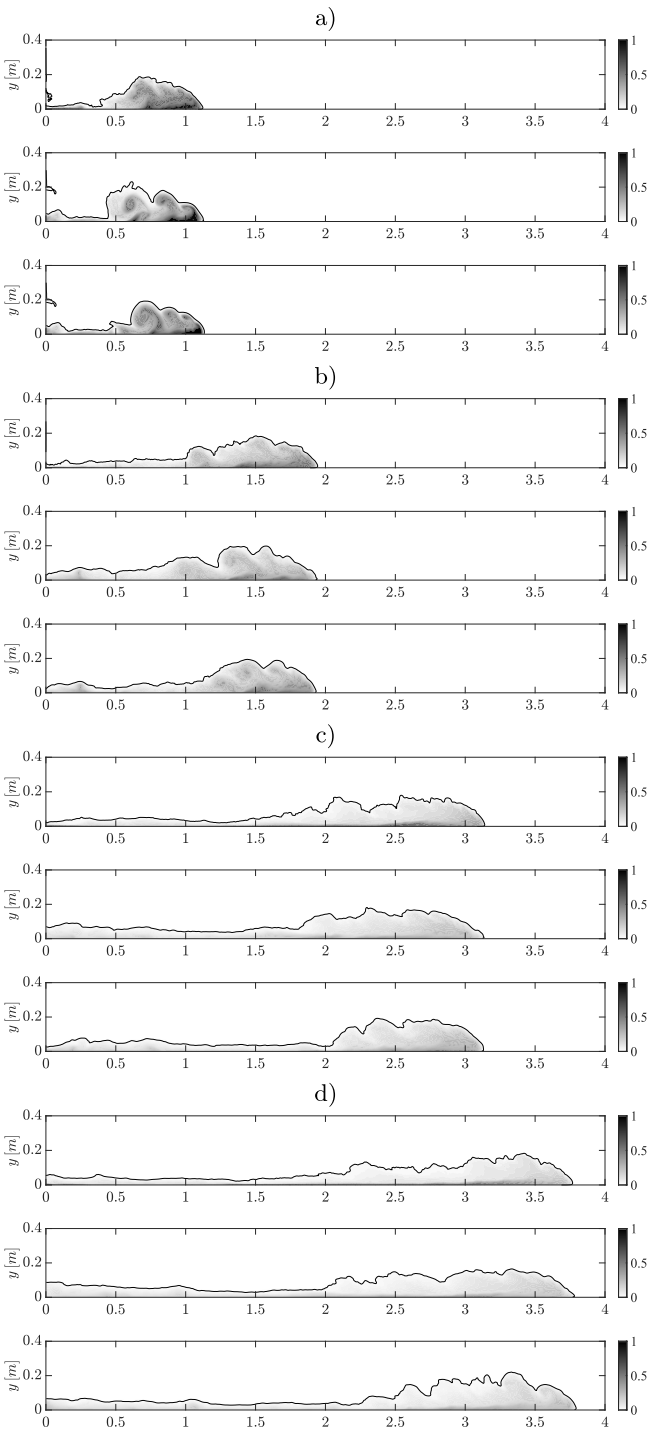


**Fig. 11.** $\langle \rho^* \rangle$ fields, a confrontation between HR-FR (top), HR-WM-S (center) and HR-NR (down) at different time steps: (a) time $T^* = 23.8$, (b) time $T^* = 47.6$, (c) time $T^* = 91.8$ and (d) time $T^* = 119$.

#### 4.2.4. Entrainment

The use of a coarse near-wall grid inevitably affects the spatial discretization within the computational domain, particularly in the interface region between the denser fluid and the ambient environment, where most of the mixing occurs. Consequently, it is essential to evaluate the model's capability to accurately capture both the entrainment process and the characteristic density of the gravity current in space and time.

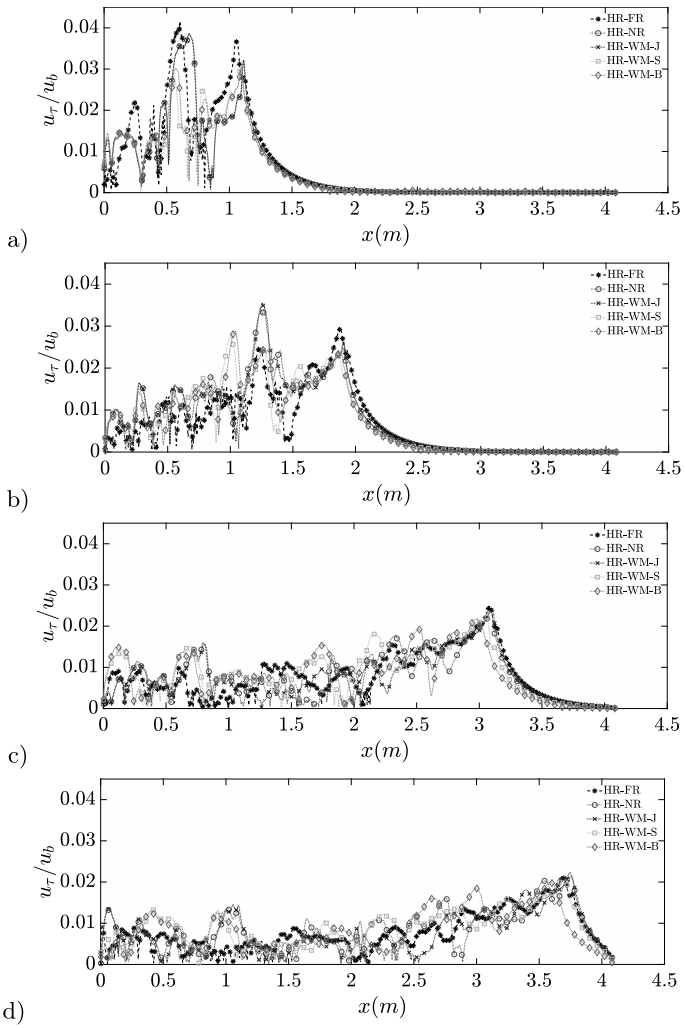


**Fig. 12.** Dimensionless friction velocity at different times, a confrontation between HR-FR and the HR-WM cases: (a) time $T^*$ = 23.8, (b) time $T^*$ = 47.6, (c) time $T^*$ = 91.8, and (d) time $T^*$ = 119.

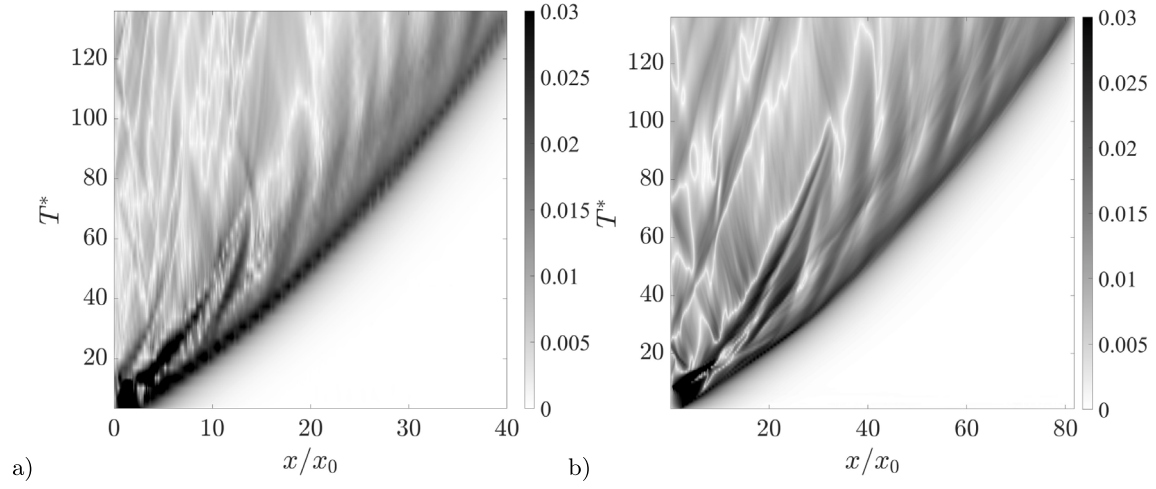


**Fig. 13.** Hövmoller diagrams of the dimensionless friction velocity field $\langle u_\tau \rangle / u_b$ for HR-FR (a) and HR-WM-S (b) cases.

Fig. 14a shows the time evolution of the averaged density over the complete gravity current at every instance of time (with the isopycnal threshold value $\langle \rho^* \rangle = 0.02$).

During the slumping phase, the coarse-grid cases tend to diverge from the reference case due to reduced mixing, resulting from the lower accuracy in representing Kelvin–Helmholtz structures (see 11a) and the current tail. In the transition from the slumping phase to the self-similar phase, the results for the HR-NR and HR-WM-J cases are consistent with those of the resolved case. In contrast, for the cases with increased near-bottom eddy viscosity (HR-WM-S and HR-WM-B), a greater deviation is

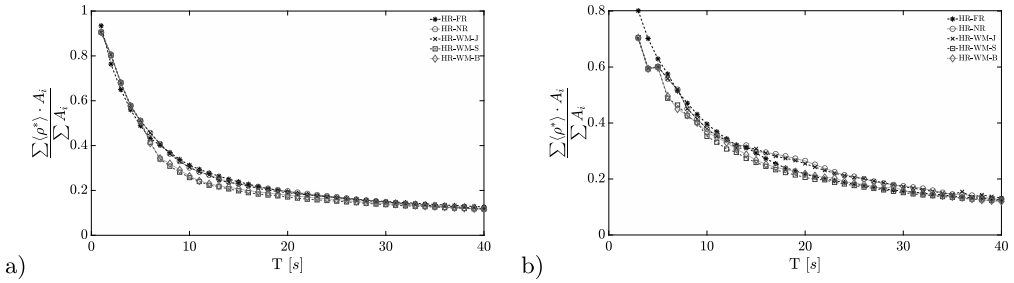


**Fig. 14.** Evolution in time of the dimensionless surface mass of the total current (a) and of the head (b).

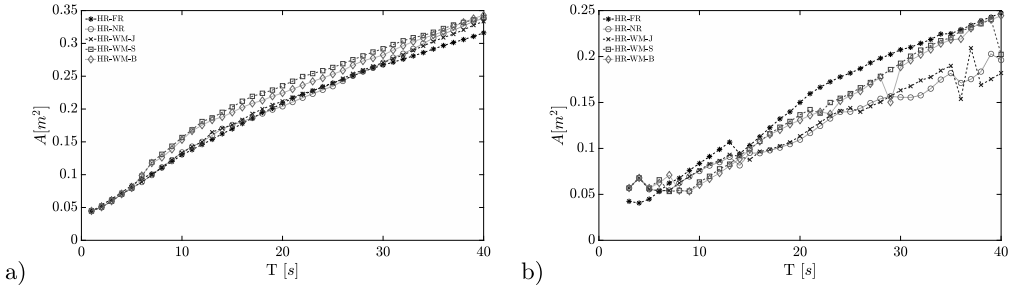


**Fig. 15.** Evolution in time of the total current Area (a) and of the head Area (b).

observed, with an integral density value significantly lower than in the other cases; only in the final phase the profiles tend to realign with the other solutions. This discrepancy can be attributed to the fact that the wall models are applied to the entire current, including the tail region, where they are likely not suitable.

As evidence of this, see Fig. 14b, where the integral density is shown only in the head region, as identified in 4.2.1. It should be noted that, for the figure, as well as for the subsequent figures referring to the head of the current, the initial seconds are not shown, as the head is not yet fully defined. The results show that, during the slumping phase and the transition to the self-similar phase, all coarse grid cases produce excessive mixing (and consequently a lower current density). Subsequently, it is observed that, in the self-similar phase, the cases employing viscosity-based wall models more accurately reproduce the reference case. As mentioned in the flow topology analysis (see Section 4.2.2), additional cases were run with even coarser grids in the $x$-direction, which exhibit an overall slowing of the current. In these cases, the reduction in current density during the slumping and transition phases is even more pronounced. This suggests that the coarse meshes are unable to adequately capture the mixing processes between saline and freshwater during the slumping phase, not because of the model itself, but due to insufficient spatial resolution. This leads probably to an excessive decrease in horizontal pressure gradients, and consequently, to a reduction in the front velocity, which is not subsequently recovered.

The observations described above can also be related to the dimensions of the gravity current. Fig. 15a and b show the area of the current enclosed by the reference value $\langle\rho^*\rangle = 0.02$, for the entire current and for the head only, respectively. Fig. 15a clearly shows that the HR-WM-S and HR-WM-B cases deviate markedly from the reference case during the transition from the slumping to the self-similar phase, exhibiting a larger area and, consequently, a lower density; subsequently, they maintain a slope similar to that observed for the resolved case. By contrast, the HR-NR and HR-WM-J cases tend to deviate from the resolved case only in the final part of the self-similar phase. Considering only the head region (Fig. 15b), it can be noted that the HR-WM-S and HR-WM-B cases generally display behavior closer to that of the resolved case.

The behavior described in terms of current density and area can also be effectively quantified in terms of entrainment as performed in the reference study (Ottolenghi et al., 2016b). At time $t_0 = 0$, we define $V_0$ as the initial volume of the gravity current. At a successive time, $t_i = t_0 + \Delta t$, the volume of the current will increase by a quantity $\Delta V_i$ with respect to $V_0$, due to entrainment. This increment can be defined as:

$$\Delta V_i = (A_i - A_0)d \tag{29}$$

where $d$ denotes the spanwise length of the channel, while $A_i$ is the area below the isopycnal $\langle\rho^*\rangle = 0.02$ in a x-y plane. $A_0$ is the area of the gravity current at $t_0$, i.e. $A_0 = Hx_0$. Starting from $\Delta V_i$, it is possible to calculate the bulk entrainment discharge as:

$$Q_{ei} = \frac{\Delta V_i}{\Delta t_i} \tag{30}$$

and the bulk entrainment velocity for every time step as:

$$W_{ei} = \frac{Q_{ei}}{S_i} \tag{31}$$

where $S_i$ is the interface between the two fluids, and can be estimated as $S_i = d \cdot x_f$. Lastly, a dimensionless number for the entrainment can be defined as:

$$E_i = \frac{W_{ei}}{2U_{i-bulk}} \tag{32}$$

where the bulk entrainment velocity is made non-dimensional with the velocity scale $U_{i-bulk} = V_1 - V_2$ (Ottolenghi et al., 2016b), with $V_1$ the bulk velocity of the density current, calculated as $(x_f - x_0)/(t_f - t_0)$, (where $t_f$ denotes the time in which the gravity current has reached the position $x_f$) and $V_2$ is the bulk velocity of the ambient fluid.

Fig. 16a shows the entrainment as a function of the front position of the gravity current. Entrainment is highest during the initial phase, particularly in the slumping phase, where Kelvin–Helmholtz structures promote intense mixing between the current and the ambient fluid. As the flow evolves towards the self-similar phase, entrainment gradually decreases, following an approximately exponential trend.

The trends previously identified for density and current area are confirmed. During the transition from the slumping to the self-similar phase, the HR-WM-S and HR-WM-B cases are characterized by substantial entrainment. Subsequently, in the remaining part of the self-similar phase, entrainment decreases and tends to align with that of the HR-FR case, although it remains consistently higher. The HR-NR and HR-WM-J

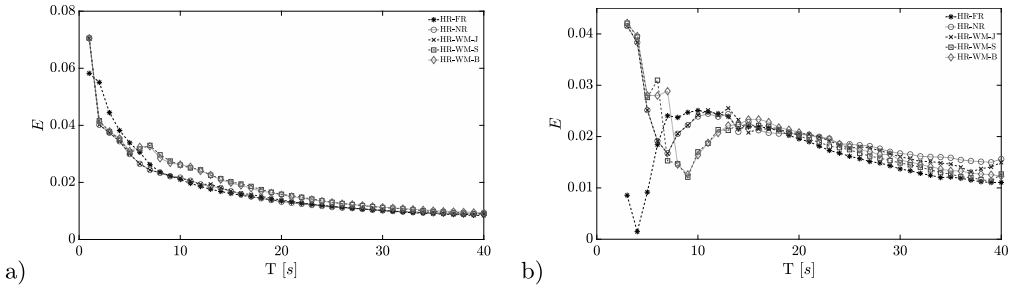


**Fig. 16.** Evolution in time of the total current Entrainment (a) and of the head (b).

cases remain in agreement with the reference case throughout the self-similar phase. The overall behavior of the coarse-grid cases changes, however, when considering only the head of the current (see Fig. 16b). In this region, during the self-similar phase, the cases with increased eddy viscosity tend to exhibit behavior more consistent with that of the HR-FR case. As the current evolves, the HR-NR case is observed to diverge increasingly from the reference case.

#### 4.2.5. Near-wall region

The analysis of the near-wall region provides valuable insights into the streamwise velocity fluctuations ($u' = u - \langle u \rangle$) within this zone. Fig. 17 presents these fluctuations at the first computational cell above the bottom wall, comparing the results of HR-FR (top), HR-WM-S (center), and HR-NR (bottom) at four distinct time instances.

In the HR-FR case, near the head of the current, elongated turbulent structures are clearly identifiable (Fig. 17). These streaks are typical of wall-bounded flows (Pope, 2015) and are commonly observed during the evolution of gravity currents as well (see Ooi et al., 2009; Ottolenghi et al., 2017).

These coherent structures suggest that bed erosion is primarily driven along their longitudinal axes, with their fluctuations indicating regions of elevated shear stress. As the flow progresses downstream, these structures progressively dissipate, eventually vanishing within the tail of the current. This spatial decay pattern, corroborated by the distribution of friction velocity (Fig. 12), implies that the maximum erosive potential is concentrated at the leading edge of the current.

The presence of these specific structures provides insight into the current's ability to entrain bed particles along their paths, offering a better understanding of the sediment redistribution caused by this type of flow. Furthermore, the observed shortening of these structures over time indicates a reduction in the erosive potential of the current, as it evolves from the slumping phase (Fig. 17a) to the self-similar phase (Fig. 17b,c,d). Regarding the comparison with the coarse grid cases, Fig. 17a shows that during the slumping phase, the HR-NR struggles to capture the majority of velocity fluctuations near the current head, in contrast to the reference case. As a result, the simulation fails to accurately reproduce the erosive potential of the current during this phase. Conversely, the HR-WM-S case exhibits improved performance in this region. Although HR-WM-S reproduces the characteristic elongated structures, the near-wall region reveals structures that are larger in the spanwise direction. This is a common effect of wall functions, due to the resolution, artificially amplified turbulent structures develop near the wall, exhibiting unphysical characteristics in the horizontal directions (Piomelli, 2008; Cabot and Moin, 2000).

At later time instances, the HR-NR configuration exhibits enhanced capability in reproducing velocity fluctuations, particularly in the vicinity of the current head.

The behavior approaches that observed for the HR-WM-S case, with both deviating from the resolved case in terms of the spanwise extent of these structures. It is also evident that the coarse grid cases exhibit high fluctuation levels even in the tail of the current, compared to the HR-FR case. This aspect is consistent with the greater tail thickness observed in Fig. 11 and with the friction velocity shown in Fig. 12.

## 5. Conclusions

Gravity currents play an important role in the dynamics of environmental flows. Their behavior is governed by complex physics, primarily driven by turbulent mixing between fluids of different densities and interactions with the bottom boundary. Accurately capturing their dynamics from a numerical perspective requires the use of high-resolution approaches, such as Large Eddy Simulation. However, the substantial computational cost of such methods, particularly near the wall, limits their practical applicability to domains and dimensionless parameters characteristic of environmental flows.

To address this limitation, the present study investigates the performance of implementing coarse grid, with and without wall models, in representing gravity currents. The analysis was carried out using a lock-exchange configuration at a Reynolds number of 136,000. First, a wall-resolved Large Eddy Simulation was performed to provide reference data. Subsequently, four cases were evaluated on a coarser grid: two based on modifications of eddy viscosity, one based on modification of eddy diffusivity, one skipping the viscous sub-layer solution.

Overall, the results obtained are qualitatively similar to the reference case, except for the case run with the Blended wall model. The temporal and spatial evolution of the gravity current's head shape is well captured. Although, in the cases without eddy viscosity intensification, it appears more compact. Moreover, a thicker tail is observed in all cases compared to the reference case.

Regarding the temporal evolution of the current front, the average relative error with respect to the reference case is on the range 0.25%–2.70%, with the lower error for the not resolved and the Spalding case. All the cases analyzed exhibit similar behavior during the slumping phase, with an error on the order of 1%, and then deviate during the self-similar phase. In particular, it is observed that the case employing Spalding's wall model tends to reduce the error relative to the reference case as time progresses. It is also noted that, towards the end of the self-similar phase, the resolved case exhibits a logarithmic region that appears well-defined and stable.

Due to the grid resolution in the wall-normal direction, the various coarse grid cases are unable to capture the turbulent structures that develop near the bottom, which are instead observed in the resolved case; therefore, they may be deficient in accurately representing sediment resuspension. However, during the self-similar phase, the friction velocity appears to be well reproduced, at least in the head region of the gravity current. This observation is especially valid in the final phase for the case run using Spalding's wall model.

In the results presented above, no significant differences were observed between the cases with and without a wall model (excluding the Blended case). However, substantial differences are observed with respect to entrainment, mean density, and the area of the gravity current. The not resolved case and the case with modified eddy diffusivity are much closer to the reference case, when considering the gravity current in its entirety. The behavior changes when focusing solely on the gravity current head: in this region, the cases with eddy viscosity intensification exhibit the best results as time progresses. This behavior

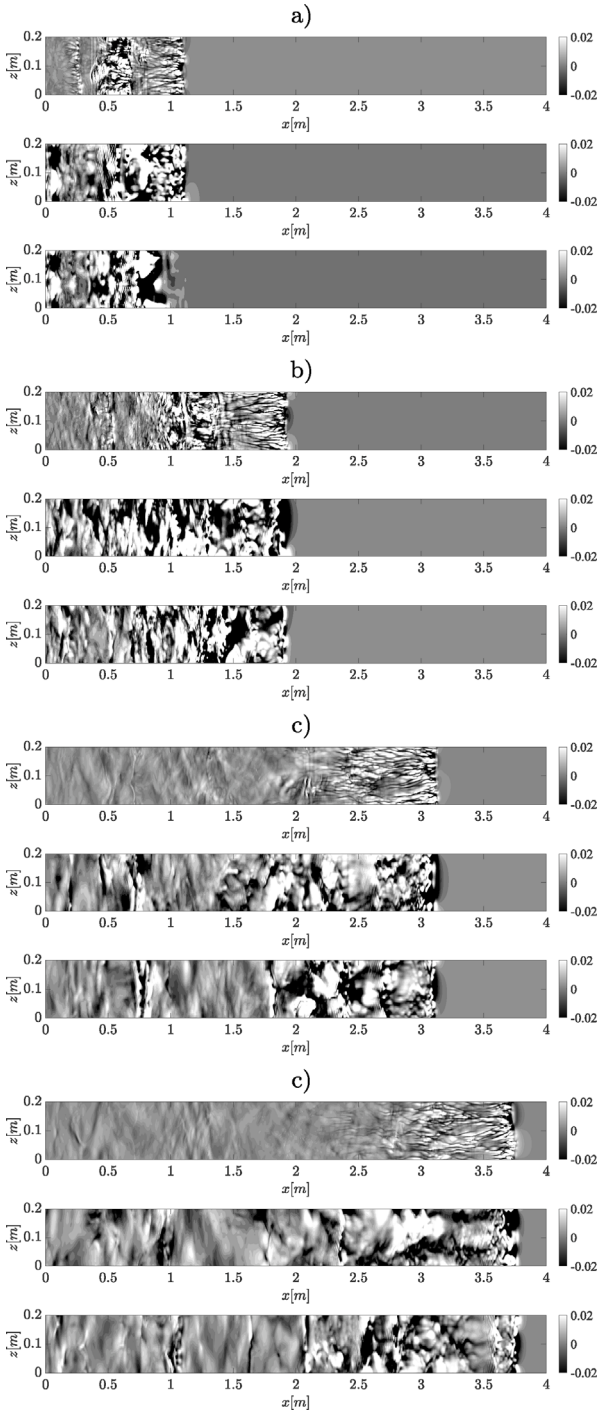


**Fig. 17.** Dimensionless velocity fluctuation at the first cell above the bottom wall, at different times, a confrontation between HR-FR case (top), HR-WM-S case (center) and HR-NR case (down): (a) time $T^* = 23.8$, (b) time $T^* = 47.6$, (c) time $T^* = 91.8$, (c) time $T^* = 119$.

can be attributed to the fact that, only in the head of the current develops a velocity profile that aligns with the assumptions of the wall models.

In conclusion, the analyzed cases with coarse grid seem to be effective in capturing the dynamics of gravity currents, particularly during the self-similar phase of the flow evolution. The most accurate results were obtained using the Spalding model, likely due to its ability to fully characterize the near-wall velocity profile, including the viscous sub-layer.

The computational advantage is also evident: the mesh resolution employed is approximately one order of magnitude lower than that needed for the fully resolved simulations. Furthermore, the reduced spatial resolution allows for larger time steps while still satisfying the numerical stability criteria, thereby decreasing the total number of iterations and contributing to overall computational efficiency.

In principle, the methodology with wall model lends itself to being extended to a variety of cases beyond the one analyzed, such as three-dimensional gravity currents on inclined planes (Ross et al., 2002; Zgheib et al., 2016; Dai and Huang, 2020), and to geometries different from the circular one (Zgheib et al., 2015). The subgrid-scale model, in fact, does not require the presence of homogeneous directions. Furthermore, the wall model, based on a local modification of the eddy viscosity, incorporates a wall profile that accounts for the viscous sublayer, the buffer layer, and the logarithmic region, thus enabling the simulation of flows characterized by varying spatial dynamics. However, extending the approach to these types of configuration would require an appropriate verification and calibration procedure. In the specific case analyzed, future research activities could focus on improving the calibration of wall models through a more detailed analysis of the near-wall behavior in the head region of the gravity current, while differentiating the wall-function behavior in the tail. Subsequently, the performance of even coarser grids, which currently do not yield satisfactory results, could be re-evaluated.

## CRediT authorship contribution statement

**Antonio Ammendola:** Writing – review & editing, Writing – original draft, Visualization, Methodology, Investigation. **Michele Rebesco:** Writing – review & editing, Conceptualization. **Federico Falcini:** Writing – review & editing, Conceptualization. **Stefano Salon:** Writing – review & editing, Conceptualization. **Federico Roman:** Writing – review & editing, Writing – original draft, Supervision, Methodology, Investigation, Data curation, Conceptualization.

## Declaration of competing interest

The authors declare that they have no known competing financial interests or personal relationships that could have appeared to influence the work reported in this paper.

## Acknowledgments

This work is funded by the National Recovery and Resilience Plan project TeRABIT (Terabit network for Research and Academic Big data in Italy - IR0000022 - PNRR Missione 4, Componente 2, Investimento 3.1 CUP I53C21000370006) in the frame of the European Union - NextGenerationEU funding.

The authors also acknowledge the support of the CINECA award under the ISCRA initiative for the availability of high-performance computing resources and support.

## Data availability

Data will be made available on request.

## References


Adduce, C., Sciortino, G., Proietti, S., 2012. Gravity currents produced by lock exchanges: Experiments and simulations with a two-layer shallow-water model with entrainment. J. Hydraul. Eng. 138, 111–121.

Armenio, V., Sarkar, S., 2002. An investigation of stably stratified turbulent channel flow using large-eddy simulation. J. Fluid Mech. 459, 1–42.

Boegman, L., 2009. Currents in stratified water bodies 2: Internal waves. In: Encyclopedia of Inland Waters. pp. 539–558.

Buchhave, P., 1992. Particle image velocimetry—status and trends. Exp. Therm. Fluid Sci. 5, 586–604.

Cabot, W., Moin, P., 2000. Approximate wall boundary conditions in the large-eddy simulation of high Reynolds number flow. Flow Turbul. Combust. 63, 269–291.

Chapman, D., 1979. Computational aerodynamics development and outlook. AIAA J. 17, 1293–1313.

Chowdhury, M., Testik, F., 2014. A review of gravity currents formed by submerged single-port discharges in inland and coastal waters. Env. Fluid Mech. 14, 265–293.

Comte, F., Lesieur, M., 1996. Large-eddy simulation of transition to turbulence in a boundary layer developing spatially over a flat plate. J. Fluid Mech. 326, 1–36.

Dai, A., Huang, Y.-L., 2020. Experiments on gravity currents propagating on unbounded uniform slopes. Env. Fluid Mech. 20, 1637–1662. http://dx.doi.org/10.1007/s10652-020-09758-2.

De Vanna, F., Bernardini, M., Picano, F., Benini, E., 2022. Wall-modeled LES of shock-wave/boundary layer interaction. Int. J. Heat Fluid Flow. 98, 109071, https://doi.org/10.1016/j.ijheatfluidflow.2022.109071.

Fan, G., Liu, Y., Zhao, W., Wan, D., 2024. Effect of wall stress models and subgrid-scale models for flow past a cylinder at Reynolds number 3900. Phys. Fluids 36, 015152, https://doi.org/10.1063/5.0181469.

Fannelop, T., Waldman, G., 1972. Dynamics of oil slicks. AIAA J. 10, 506–510.

Ferziger, J., Perić, M., Street, R., 2020. Computational Methods for Fluid Dynamics. Springer.

Franck, N., Ducros, F., 1999. Subgrid-scale stress modelling based on the square of the velocity gradient tensor. Flow Turbul. Combust. 62, 183–200.

Georgoulas, A., Angelidis, P., Panagiotidis, T., Kotsovinos, N., 2010. 3D numerical modelling of turbidity currents. Env. Fluid Mech. 10, 603–635.

Gong, C., Wang, Y., Rebesco, M., Salon, S., Steel, R., 2018. How do turbidity flows interact with contour currents in unidirectionally migrating deep-water channels? Geology 46, 551–554, https://doi.org/10.1130/G40204.1.

Goodarzi, D., Lari, K., Khavasi, E., Abolfathi, S., 2020. Large eddy simulation of turbidity currents in a narrow channel with different obstacle configurations. Sci. Rep. 10, 12814.

Härtel, C., Meiburg, E., Necker, F., 2000. Analysis and direct numerical simulation of the flow at a gravity-current head. Part 1. Flow topology and front speed for slip and no-slip boundaries. J. Fluid Mech. 418, 189–212.

Heerema, C., Cartigny, M., Jacinto, R., Simmons, S., Apprioual, R., Talling, P., 2022. How distinctive are flood-triggered turbidity currents? J. Sediment. Res. 92, 1–11.

Hogg, C., Pietrasz, V., Ouellette, N., Koseff, J., 2015. Dispersion and transport of hypersaline gravity currents in the presence of internal waves at a pycnocline. pp. OS11A–2005.

Huppert, H., Simpson, J., 1980. The slumping of gravity currents. J. Fluid Mech. 99, 785–799, https://doi.org/10.1017/S0022112080000894.

Inghilesi, R., Adduce, C., Lombardi, V., Roman, F., Armenio, V., 2018. Axisymmetric three-dimensional gravity currents generated by lock exchange. J. Fluid Mech. 851, 507–544.

Jayatilleke, C., 1966. The influence of Prandtl number and surface roughness on the resistance of the laminar sub-layer to momentum and heat transfer.

Kneller, B., Buckee, C., 2000. The structure and fluid mechanics of turbidity currents: a review of some recent studies and their geological implications. Sedimentology 47, 62–94, https://doi.org/10.1046/j.1365-3091.2000.047s1062.x.

Kuhlbrodt, T., Griesel, A., Montoya, M., Levermann, A., Hofmann, M., Rahmstorf, S., 2007. On the driving processes of the Atlantic meridional overturning circulation. Rev. Geophys. 45.

Kyrousi, F., Leonardi, A., Roman, F., Armenio, V., Zanello, F., Zordan, J., Juez, C., Falcomer, L., 2018. Large Eddy Simulations of sediment entrainment induced by a lock-exchange gravity current. Adv. Water Resour. 114, 102–118.

Maggi, M., Adduce, C., Negretti, M., 2022. Lock-release gravity currents propagating over roughness elements. Env. Fluid Mech. 22, 383–402.

Maggi, M., Negretti, M., Hopfinger, E., Adduce, C., 2023. Turbulence characteristics and mixing properties of gravity currents over complex topography. Phys. Fluids 35, 016607.

Meiburg, E., Kneller, B., 2010. Turbidity currents and their deposits. Annu. Rev. Fluid Mech. 42, 135–156.

Menter, F., 1994. Two-equation eddy-viscosity turbulence models for engineering applications. AIAA J. 32, 1598–1605.

Miramontes, E., Eggenhuisen, J., Jacinto, R., Poneti, G., Pohl, F., Normandeau, A., Campbell, D., Hernández-Molina, F., 2020. Channel-levee evolution in combined contour current–turbidity current flows from flume-tank experiments. Geology 48, 353–357.

Mukha, T., Rezaeiravesh, S., Liefvendahl, M., 2019. A library for wall-modelled large-eddy simulation based on OpenFOAM technology. Comput. Phys. Comm. 239, 204–224, https://doi.org/10.1016/j.cpc.2019.01.016.

Nogueira, H., Adduce, C., Alves, E., Franca, M., 2013. Analysis of lock-exchange gravity currents over smooth and rough beds. J. Hydraul. Res. 51, 417–431.

Nogueira, H.I.S., Adduce, C., Alves, E., Franca, M.J., 2014. Dynamics of the head of gravity currents. Environ. Fluid Mech. 14, 519–540. http://dx.doi.org/10.1007/s10652-013-9315-2.

Normandeau, A., Campbell, D., Cartigny, M., 2019. The influence of turbidity currents and contour currents on the distribution of deep-water sediment waves offshore Eastern Canada. Sedimentology 66, 1746–1767.

Ooi, S., Constantinescu, G., Weber, L., 2009. Numerical simulations of lock-exchange compositional gravity currents. J. Fluid Mech. 635, 361–388.

Ottolenghi, L., Adduce, C., Inghilesi, R., Armenio, V., Roman, F., 2016a. Entrainment and mixing in unsteady gravity currents. J. Hydraul. Res. 54, 541–557.

Ottolenghi, L., Adduce, C., Inghilesi, R., Roman, F., Armenio, V., 2016b. Mixing in lock-release gravity currents propagating up a slope. Phys. Fluids 28, 056604.

Ottolenghi, L., Adduce, C., Roman, F., Armenio, V., 2017. Analysis of the flow in gravity currents propagating up a slope. Ocean. Model. 115, 1–13.

Pelmard, J., Norris, S., Friedrich, H., 2018. LES grid resolution requirements for the modelling of gravity currents. Comput. & Fluids 174, 256–270.

Piomelli, U., 2001. Wall-layer models for large-eddy simulations.

Piomelli, U., 2008. Wall-layer models for large-eddy simulations. Prog. Aerosp. Sci. 44, 437–446.

Pope, S., 2015. Turbulent Flows. Cambridge Univ. Press.

Rebesco, M., Hernández-Molina, F., Van Rooij, D., Wåhlin, A., 2014. Contourites and associated sediments controlled by deep-water circulation processes: State-of-the-art and future considerations. Mar. Geol. 352, 111–154.

Ross, A.N., Linden, P.F., Dalziel, S.B., 2002. A study of three-dimensional gravity currents on a uniform slope. J. Fluid Mech. 453, 239–261. http://dx.doi.org/10.1017/S0022112001006899.

Rottman, J., Simpson, J., 1983. Gravity currents produced by instantaneous releases of a heavy fluid in a rectangular channel. J. Fluid Mech. 135, 95–110.

Sequeiros, O., 2012. Estimating turbidity current conditions from channel morphology: A froude number approach. J. Geophys. Res. Ocean. 117.

Simpson, J., 1997. Gravity Currents in the Environment and the Laboratory. Cambridge University Press.

Spalding, D., 1961. A single formula for the law of the wall. J. Appl. Mech. 28, 455–458.

Stancanelli, L., Musumeci, R., Cavallaro, L., Foti, E., 2017. A small scale pressure retarded osmosis power plant: Dynamics of the brackish effluent discharge along the coast. Ocean Eng. 130, 417–428.

Temmerman, L., Leschziner, M.A., Mellen, C.P., Fröhlich, J., 2003. Investigation of wall-function approximations and subgrid-scale models in large eddy simulation of separated flow in a channel with streamwise periodic constrictions. J. Heat Fluid Flow. 24 (2), 157–180. http://dx.doi.org/10.1016/S0142-727X(02)00222-9.

Tokyay, T., Constantinescu, G., Meiburg, E., 2011. Lock-exchange gravity currents with a high volume of release propagating over a periodic array of obstacles. J. Fluid Mech. 672, 570–605.

Ungarish, M., 2009. An Introduction To Gravity Currents and Intrusions, first ed. Vol. 512, Chapman and Hall/CRC, New York, ISBN: 978-0-429-14343-4, p. eBook. http://dx.doi.org/10.1201/9781584889045.

Westerweel, J., Elsinga, G.E., Adrian, R.J., 2013. Particle image velocimetry for complex and turbulent flows. Annu. Rev. Fluid Mech. 45, 369–396, https://doi.org/10.1146/annurev-fluid-120710-101204.

Wu, C., Ouyang, H., 2020. Flow morphology in bottom-propagating gravity currents over immersed obstacles. AIP Adv. 10, 115103.

Zgheib, N., Bonometti, T., Balachandar, S., 2015. Direct numerical simulation of cylindrical particle-laden gravity currents. Comput. Fluids 123, 23–31. http://dx.doi.org/10.1016/j.compfluid.2015.09.001.

Zgheib, N., Ooi, A., Balachandar, S., 2016. Front dynamics and entrainment of finite circular gravity currents on an unbounded uniform slope. J. Fluid Mech. 801, 322–352. http://dx.doi.org/10.1017/jfm.2016.325.